



Flow-boiling canopy wick capillary-viscous limit

Tong Kyun Kim^{a,1}, Julio Ferreira^{b,1}, HangJin Jo^{a,*}, Massoud Kaviany^{a,b,*}

^a Division of Advanced Nuclear Engineering, Pohang University of Science and Technology, Pohang 37673, Republic of Korea

^b Department of Mechanical Engineering, University of Michigan, Ann Arbor, MI 48109, USA

ARTICLE INFO

Article history:

Received 21 July 2021

Revised 21 August 2021

Accepted 21 September 2021

Keywords:

Flow boiling canopy wick
Enhanced critical heat flux
Capillary-viscous dryout limit
Hydrodynamic dryout limit
Perforated canopy wick with levees
Extreme heat flux
Enhanced heat transfer coefficient
Monolayer
Bimodal bilayer evaporator wick

ABSTRACT

It was predicted that the perforated, leveed flow-boiling canopy wick (FBCW) can significantly increase the hydrodynamic instability limit of the flow boiling [1,2]. The perforations represent and modulate the vapor columns in the boiling crises hydrodynamic stability theory. The lower capillary-viscous limit, governed by the evaporator wick maximum capillary pressure and the viscous drag within the three-dimensional composite wick, may control the actual dryout performance. Saturated-water flow-boiling (one atm) experiment results are presented employing an FBCW, created from sintered-copper particles, with and without the hydrodynamic-stabilizing levees. The bimodal bilayer evaporator wick allows for sufficiently large maximum capillary pressure and permeability, compared to the monolayer wick. The experimental results indicate that the levees can increase the critical heat flux (CHF) over that without levees, whereas the existing maximum capillary pressure controls disallow achieving this larger hydrodynamic heat flux limit. This capillary-viscous dryout limit is predicted by employing the minimum surface energy principles, network models, and computational fluid dynamics (CFD), in good agreement with experiments. By employing both CFD and flow visualizations, good agreement is also established between the predicted and observed two-phase hydrodynamics above the canopy wick. They indicate that although the local dryout commences downstream; however, dryout is experimentally observed when a critical fraction of the liquid supply tracks dry downstream. The measured large thermal conductance (heat transfer coefficient) is beneficial for the predictions, verifying the vapor-occupied space between the canopy and evaporator wicks.

© 2021 Elsevier Ltd. All rights reserved.

1. Introduction

Coatings reduce the surface superheat $T_s - T_{lg}$ by either assisting in increasing the nucleation sites or in creating film evaporation across thin, permeable coatings. They also enhance the capillary-viscous CHF, $q_{CHF,c-v}$, governed by the liquid-vapor hydrodynamic instability or by the capillary-viscous limit of liquid flow through porous bodies. The 3-D wick separates the liquid and vapor phases, therefore, reducing the liquid-vapor counter-flow resistance adjacent to the surface. Both the hydrodynamic and capillary limits can cause liquid choking and lead to CHF. The liquid-choking limit is predicted to occur first (the lower of the two limits), with increasing surface heat flux q . The vapor escape paths are more readily accommodated.

The departing bubbles and imbibing liquid compete at the heated surface, leading the dryout at high heat flux, such as the

hydrodynamic CHF $q_{CHF,h}$. Zuber [3] proposed that near the CHF, the vapor columns (continuous bubbles) depart from the surface as jets with the specific square arrangement (unit cell) stemming from the interaction between the Kelvin-Helmholtz and the Rayleigh-Taylor instabilities. This notion was confirmed in [4]. The pool-boiling limit description was expanded in [5]. The results from [6] imply that the hydrodynamic limit can be further enhanced by modulating the vapor jet arrangement.

In saturated flow boiling, after a threshold in liquid velocity, this $q_{CHF,h}$ becomes greater than the corresponding pool-boiling limit. This is because the axial liquid inertia can more effectively counter the deflected departing bubbles (or vapor columns in the boiling crisis hydrodynamic stability theory). Efforts were made to predict the flow-boiling hydrodynamic CHF; however, they are often empirical and cannot be expanded. The focus, therefore, shifted to describe the mechanism(s) responsible for triggering the CHF [7,8]. The interfacial lift-off model [9], based on the surface wetting, occurring with small liquid patches between long vapor patches, was closely examined in [1]. The dryout occurs when the momentum of the generated vapor overcomes the interfacial pressure force, therefore, lifting the interface, and preventing the liq-

* Corresponding authors at: Division of Advanced Nuclear Engineering, Pohang University of Science and Technology, Pohang 37673, Republic of Korea and Department of Mechanical Engineering, University of Michigan, Ann Arbor, MI 48109, USA.

E-mail addresses: jhj04@postech.ac.kr (H. Jo), kaviany@umich.edu (M. Kaviany).

¹ These authors contributed equally to this work.

Nomenclature

A	area (m ²)
b_x	systematic uncertainty
C	inertial resistance coefficient (1/m)
c_p	specific heat (J/kg-K)
D, d	diameter (m)
Fr	Froude number
g	gravity (m/s ²)
G/A	global thermal conductance (MW/m ² -K)
H, h	height (m)
Δh_{lg}	heat of evaporation (J/kg)
K	permeability (m ²)
K_r	coverage factor
k	thermal conductivity (W/m-K)
L, l	length (m)
L'_p	evaporator unit cell equivalent diameter (m)
Ma	Mach number
p	pressure (Pa)
Q	heat load (W)
q	heat flux (W/m ²)
R	derived parameter
R_e	electrical resistance (Ω)
r	radius (m)
Re	Reynolds number
r	radius (m)
s_x	random uncertainty
T	temperature ($^{\circ}$ C)
t	time (s)
U	expanded uncertainty
u	velocity (m/s), combined uncertainty
u_a	speed of sound (m/s)
$u_{l,o}$	liquid inlet velocity (m/s)
v	velocity (m/s)
V	volume (m ³), voltage (V)
W, w	width (m)
We	Weber number
x	vapor quality
X	measured parameter

Greek Symbols

δ	liquid thickness (m)
Δ	variation
ϵ	porosity
η_e	effectiveness of heat absorption
μ	viscosity (Pa-s)
ρ	density (m ³ /kg)
σ	surface tension (N/m)
θ_c	contact angle ($^{\circ}$)

Subscripts

c	capillary, curvature
ca	canopy
ch	channel
CHF	critical heat flux
$c-v$	capillary-viscous
e	evaporator
g	gas/vapor
h	hydrodynamic
l	liquid
lg	saturation
max	maximum
o	outlet
p	particle, post

per	perforation
ps	plain surface
s	surface
sh	superheat

Others

$\langle \rangle$	spatial average
*	dimensionless
CFD	Computational fluid dynamics
CHF	Critical heat flux
DI	Deionized
PEEK	Polyether ether ketone
PID	Proportional integral derivative
SE	Surface evolver
SEM	Scanning electron microscope

uid from reaching the heated surface. This interfacial lift-off model was recently expanded in [10], suggesting that the vapor generated in the wetting front behaves similarly to the columnar jets in the pool boiling. These jets are separated by a vapor wavelength. The inlet velocity can alter this critical wavelength, triggering the CHF. The forced liquid velocity, therefore, provides a CHF enhancement similar to the porous coating surface modulation in [6].

Attributable to the random and chaotic nature of the bubbles and accumulation of vapor downstream, the exact description of this two-phase flow has been challenging and lacking. To gain a more deterministic insight into the saturated flow boiling, it would help to prescribe the location of the generated and escaping vapor. The simplest rendering is with spatial periodicity. One such construct is the perforated canopy wick (termed the FBCW) with which the two-phase hydrodynamics can be explored and its $q_{CHF,h}$ extended significantly as reported in [1,2]. Experimental evidence confirms that the enhanced hydrodynamic limit may be unattainably attributable to the wick capillary-viscous dryout limit $q_{CHF,c-v}$ (i.e., $q_{CHF,c-v} < q_{CHF,h}$).

An FBCW was fabricated and assessed. The results were compared with the plain surface. The experiments include FBCW with and without the levees to empirically verify that the levees offer additional control of vapor escape [1]. The FBCW is a multicomponent porous wick, such as the canopy, separating the liquid channel from the vapor space; the posts directing the liquid toward the evaporator. The thin evaporator balances a short heat conduction path (from the heater to the evaporating meniscus), while allowing for low-pressure drop liquid spreading. Fig. 1 displays the FBCW structure with the main geometric parameters highlighted.

The subsequent presentation starts with Section 2, where the experimental setup and the test matrix are described. In Sections 3 and 4, the evaporator wick maximum capillary pressure and the wick pressure drop components are discussed. The capillary-viscous heat flux ($q_{CHF,c-v}$) limit is predicted. Sections 5 and 6 present the experimental results of phase distributions and CHF and thermal conductance enhancements, compared to the CFD predictions. Section 7 ensues with the conclusions.

2. Experiments**2.1. Flow-boiling canopy wick fabrication and experimental setup**

Fig. 2 specifies the FBCW fabrication steps, using spherical copper particles sintered in graphite molds in a furnace [6]. Three diverse spherical diameters were used, indicating 50 μ m (50–53 μ m), 100 μ m (100–106 μ m), and 150 μ m (150–160 μ m). All sintering processes were completed in two hours under Ar gas at 900 $^{\circ}$ C in a tube furnace. First, the smallest particles were sintered on a polished copper plate (Fig. 2(a)) to form the first layer of the evapo-

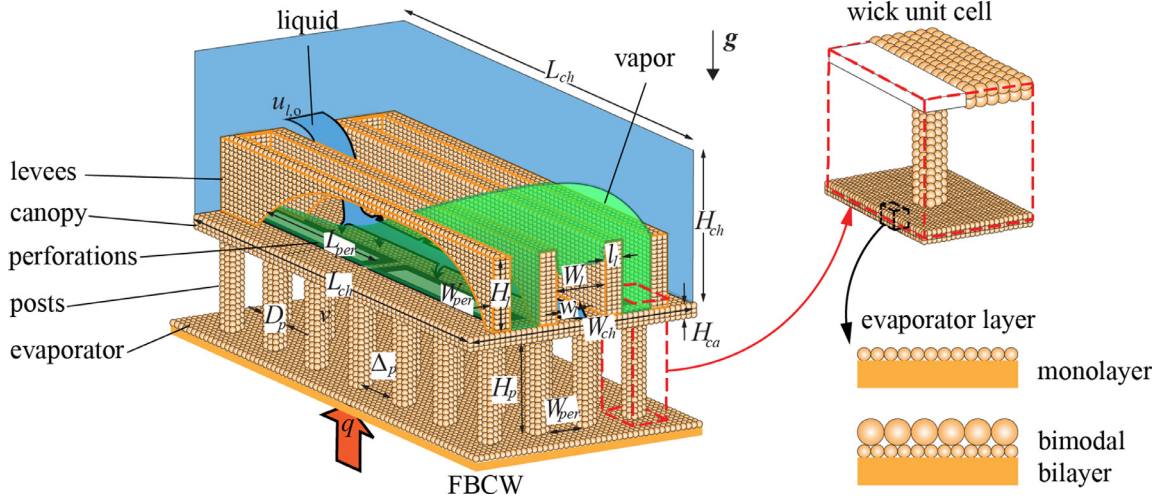


Fig. 1. Schematic of the flow-boiling canopy wick with levees, presenting the geometric parameters (The wick unit cell is detailed).

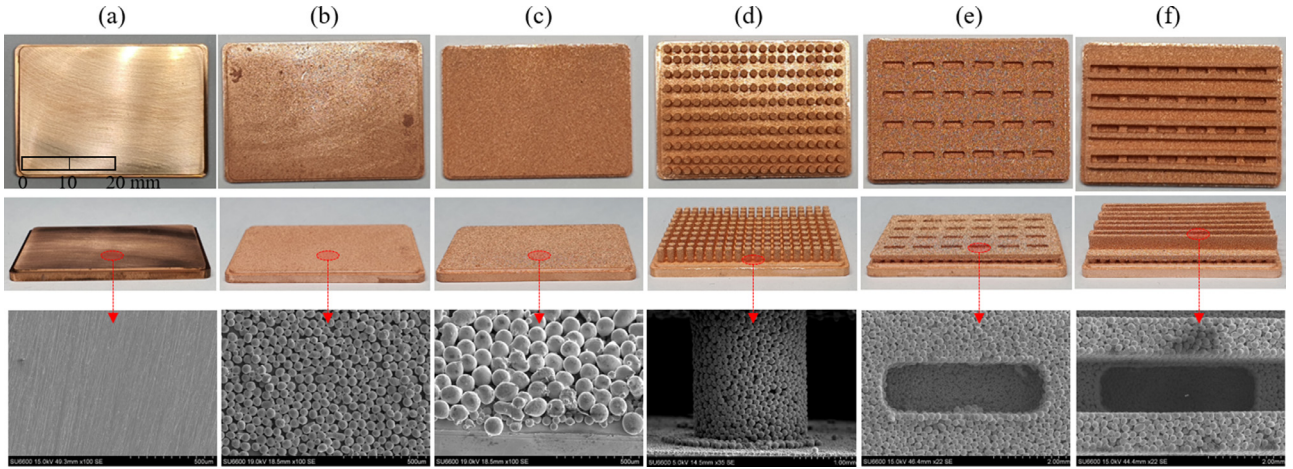


Fig. 2. Steps in the flow-boiling canopy wick fabrication. (a) Plain copper surface sintered; (b) monolayer; (c) bimodal bilayer evaporators; (d) addition of posts; (e) canopy; (f) levees. The FBCW comprises spherical copper particles sintered in graphite. The particle size for the monolayer/bilayer evaporator, posts, and perforated canopy are progressively larger to allow capillary liquid flow toward the evaporator.

rator wick (Fig. 2(b)). The particle second layer of 100 μm particles was then sintered on top of the first to form the bimodal bilayer evaporator wick (Fig. 2(c)). Graphite molds were used to form the posts (Fig. 2(d)) and the canopy. It was subsequently sintered on top of the posts (Fig. 2(e)). The addition of levees is illustrated in Fig. 2(f). The fabrication process is detailed in Appendix A.

Fig. 3(a) illustrates the test section setup. The test channel comprises aluminum. A transparent glass window was used to visualize and record the boiling phenomenon. The test channel size was $20 \times 36 \text{ mm}^2$. Cartridge heaters were inserted in the machined copper block. Two thermocouples were employed for the temperature gradient measurement in the copper block, $T_{\text{Cu},i}$. Based on these temperature measurements, the heat flux was calculated as

$$q = \frac{k_{\text{Cu}}(T_{\text{Cu},1} - T_{\text{Cu},2})}{L_{12}}, \quad (1)$$

where L_{12} is the distance between the two thermocouples. The copper substrate was connected to the jig [low thermal conductivity $k = 0.25 \text{ W/m-K}$ polyether ether ketone (PEEK)] with epoxy. The connection part between the jig and the test channel was sealed with an O-ring (Viton). Thermal interface material (TIM, $k_{\text{TIM}} = 12 \text{ W/m-K}$) was applied between the conduction heater and substrate;

their contact was adjusted by the z-aligner. The spring damper alleviated any thermal expansion of the conduction heater during the experiment.

$$T_{s,i} = T_{o,i} - \frac{q}{k_{\text{Cu}}} L_s. \quad (2)$$

The wick superheat uses the average surface temperature

$$\langle T_s \rangle - T_{lg} = \frac{1}{3} \sum_i T_{s,i} - T_{lg}. \quad (3)$$

Appendix D discusses the experimental uncertainty of these quantities.

2.2. Designs

Table 1 specifies the various FBCW designs employed in the experiments. These include eight varied evaporator designs with monolayer and bimodal bilayer evaporator wicks. Variations in the particle diameters, post heights, and low- and high-density perforations, with and without levees, were incorporated. The geometric presentation of the FBCW variations is indicated in Appendix C.

The liquid flow, heat flux (electric power), and the surface temperature ranges in the experiments are listed in Table 2.

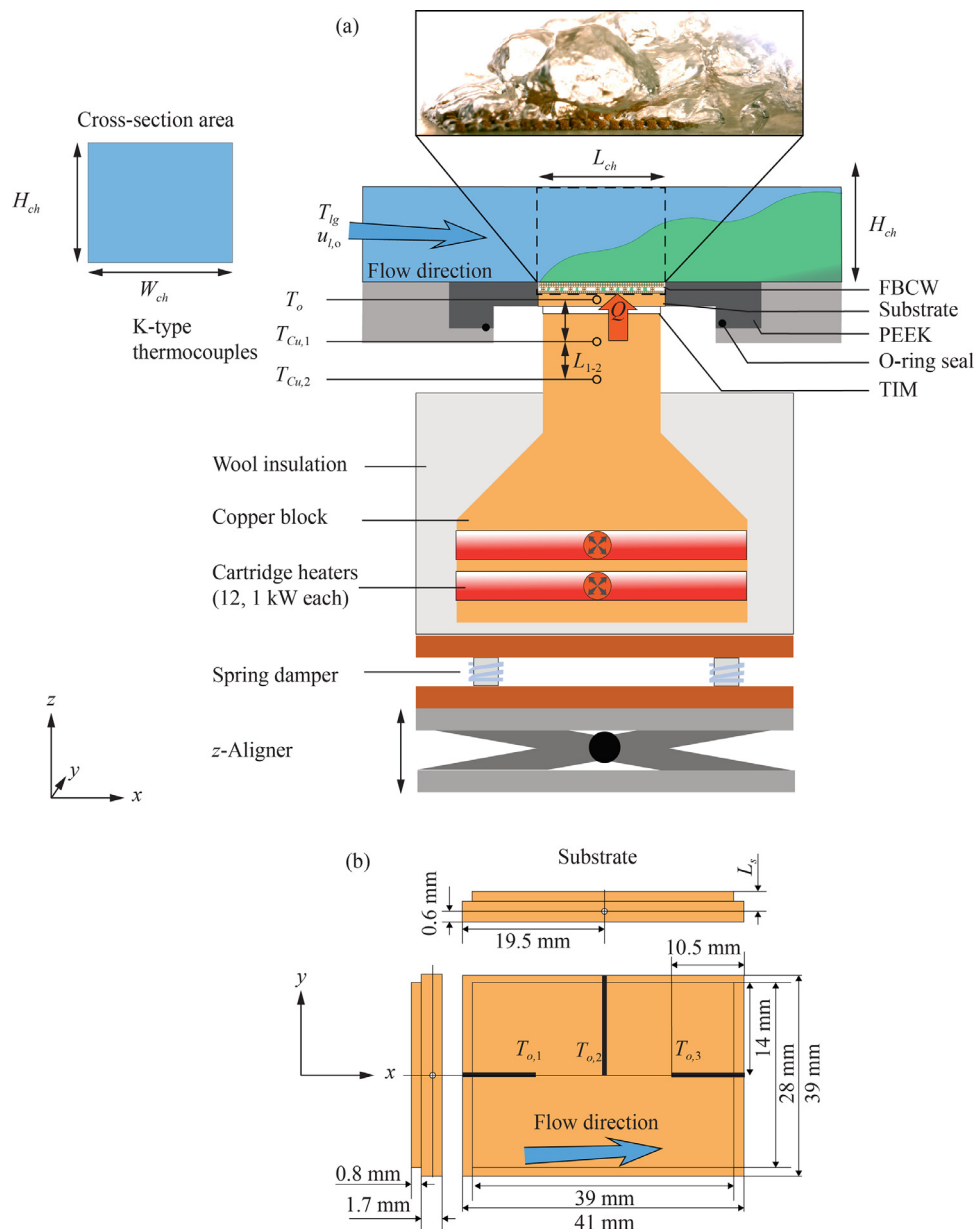


Fig. 3. (a) Schematic of the test section with the copper block and cartridge heaters; (b) Top and side views of the substrate with dimensions. The locations of the three K-type thermocouples employed to calculate the surface temperature are also indicated. Fig. 3(b) signifies the substrate with a surface area of $28 \times 39 \text{ mm}^2$ and a thickness of 2.5 mm. The surface temperature $T_{s,i}$ is measured by K-type thermocouples at three axial locations and $L_s = 1.9 \text{ mm}$ below the surface employing.

2.3. Experiment procedure

The targeted liquid flow rate was controlled with the pump and the needle valve after installing the FBCW in the test section and securing/sealing around it, ensuring direct contact with the heater block (Appendix B). The desired liquid temperature was achieved with the condenser, the preheater, and the proportional integral derivative (PID) controller. The deionized (DI) water was degassed by operating the flow-boiling loop with no load for an hour. After degassing, the heater was turned on and increasingly powered to desired heat flux in steps through the PID controller. The heat flux and the surface temperature were maintained under a steady-state for five minutes at each step. The data for each step were averaged over two minutes. When the temperature of the surface increases abruptly, the power of the heater was turned off and the test surface and the heater were separated to prevent damage. Appendix B describes the flow loop.

3. Maximum capillary pressure: role of evaporator wick particle packing

The ideal FBCW sintered, spherical particle evaporator wick, uses a single layer of unit-cell hexagonal packing on top of the heated surface, as depicted in Fig. 4(a), for a particle of diameter d_e . This flow-boiling evaporator wick design was theorized and discussed in [1] with the wick properties analyzed and predicted in [2]. Close packing of the monolayer without heterogeneity is impossible. The simplest heterogeneity model has particle vacancy in the center of the unit cell, as indicated in Fig. 4(b). As suggested, a bilayer evaporator with larger particles used in the second layer can increase the maximum capillary pressure of a heterogeneous monolayer [11]. This is presented in Fig. 4(c), termed the bimodal bilayer evaporator. The defects can occur in the monolayer and both layers of the bilayer wick. An example of aligned defect va-

Table 1
Experimental variations in the flow-boiling canopy wick design.

Design	Evaporator	d_e (μm)	d_p (μm)	H_p (mm)	W_{per} (mm)	$\Delta_{per,y}$ (mm)	d_{ca} (μm)	N_{per}	H_l (mm)
No canopy	Bilayer	50,100	150	1.3	-	-	-	-	0
FBCW	Monolayer	50	100	2.6	1.5	4.5	150	4×6	0
	Monolayer	50	100	1.3	1.5	4.5	150	4×6	0
	Monolayer	50	150	2.6	1.5	4.5	150	4×6	0
	Monolayer	50	150	1.3	1.5	4.5	150	4×6	0
	Bilayer	50,100	150	1.3	1.5	4.5	150	4×6	0
	Bilayer	50,100	150	1.3	1.5	3	150	7×6	0
FBCW with levees	Bilayer	50,100	150	1.3	1.5	3	150	7×6	5

Table 2
The ranges of electric power, heat flux, surface temperature, and inlet liquid mass flow rate in experiments.

R_e (Ω)	5.39-5.47	$T_{s,1}$ (K)	273-523	\dot{M}_l (kg/s)	0-0.72
$\Delta\varphi$ (V)	0-220	$T_{s,2}$ (K)	273-523	$u_{l,o}$ (m/s)	0-1
q (kW/m ²)	0-8000	$T_{s,3}$ (K)	273-523	L_s (mm)	1.9

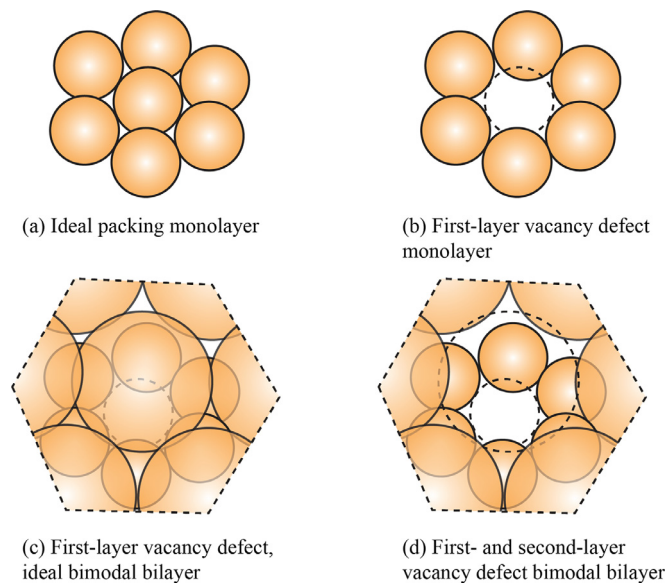


Fig. 4. Evaporator wick with (a) ideally-packed monolayer; (b) monolayer with vacancy defect; (c) bimodal bilayer with first-layer vacancy defect; (d) bimodal bilayer with first- and second-layer vacancy defect.

cancies in the first and second layers (the most critical case) is indicated in Fig. 4(d).

The meniscus anchoring and topology for the ideal monolayer are described in [2]. For the ideal bimodal bilayer wick, three meniscus-anchoring regimes exist, indicating (i) liquid above the first layer, with the meniscus anchored only to the large particles; (ii) liquid receding and transition from the second to the first layer, anchoring to both large and small particles; (iii) liquid below the second layer, with the meniscus anchored only to the small particles. Regime (i) occurs in the flooded wicks, whereas regime (iii) leads to the maximum capillary pressure in the bimodal bilayer wick. Regime (ii) corresponds to the meniscus jump, a discontinuity in the capillary pressure curve.

The vacancy defect in the second layer leaves only regime (iii) as a possibility. Provided the liquid can anchor only to the smaller particles in the bottom layer, the packing arrangements indicated in Fig. 4(b) and (d) are functionally identical for the maximum capillary pressure.

The packing arrangement and the anchoring regimes influence the wick effective properties, such as the porosity, permeability, and capillary pressure. The capillary pressure p_c is the pressure

jump across the liquid-vapor interface [12]

$$p_c = p_l - p_g = \frac{2\sigma \cos \theta_c}{r_c}, \quad (4)$$

where σ is the surface tension, θ_c is contact angle, and r_c is the radius of curvature of the liquid meniscus.

The capillary pressure was computed employing the surface evolver (SE) code [13] to simulate these regimes for the various evaporator packing arrangements; for water with a contact angle $\theta_c = 45^\circ$ [14], with smaller particle diameter d_e of 50 and 100 μm diameter. In the SE, the dimensionless pressure p_c^* was prescribed in the main calculations as a boundary condition. A new liquid meniscus topology was observed for that p_c^* by employing the surface energy minimization algorithm. By scanning p_c^* , a direct relationship between the liquid thickness and p_c^* was established. The maximum capillary pressure corresponds $p_{c,max}^*$ where a stable meniscus was detected. The dimensional $p_{c,max}$ was established from [15]

$$p_{c,max} = -\frac{p_{c,max}^* \sigma \cos \theta_c}{d_e}. \quad (5)$$

Fig. 5 signifies snapshots from the SE simulations for the monolayer with ideal packing; the vacancy defect is reflected on the right. The capillary pressure varies with the liquid thickness (maximum thickness corresponds to flooding) as indicated in the bottom left of the figure, with the average liquid thickness $\langle \delta_l \rangle$ scaled with the particle diameter d_e . The ideally-packed monolayer wick had a maximum capillary pressure $p_{c,max} = 16.2$ kPa; this is desirable but could not be achieved in experiments. The vacancy defects significantly reduced the maximum capillary pressure compared to the ideal packing, because the liquid meniscus is stretched over a large length between the anchoring points, reducing the principal radii of curvature. For the modeled monolayer with a vacancy defect, the computed maximum capillary pressure was $p_{c,max} = 2.32$ kPa, therefore, extensive loss of curvature capillarity was established.

The large particles in the ideal bimodal bilayer packing settled into the lower layer, occupying the vacancies, slightly compensated for the capillary pressure reduction. The maximum capillary pressure for the ideal bimodal bilayer packing with first-layer vacancy defects was $p_{c,max} = 2.92$ kPa.

Vacancy defects in the second layer, aligning with the defects in the first layer, (Fig. 4(d)), nullify the effectiveness of the additional layer of larger particles, therefore, reducing the maximum capillary pressure identical to that of the vacancy-defect monolayer. An example of these aligned vacancy defects in the first layer is indicated in the scanning electron microscope (SEM) micrograph at the top left of Fig. 5.

In Fig. 5, the unit-cell models of defects are highlighted. Predictions indicate variations of capillary pressure with scaled liquid thickness for the monolayer with and without defect, and for bimodal bilayer with a defect in the first layer and second layer. The snapshots of the SEM simulations on the right indicate the meniscus anchoring and its topology for all cases. The results are for

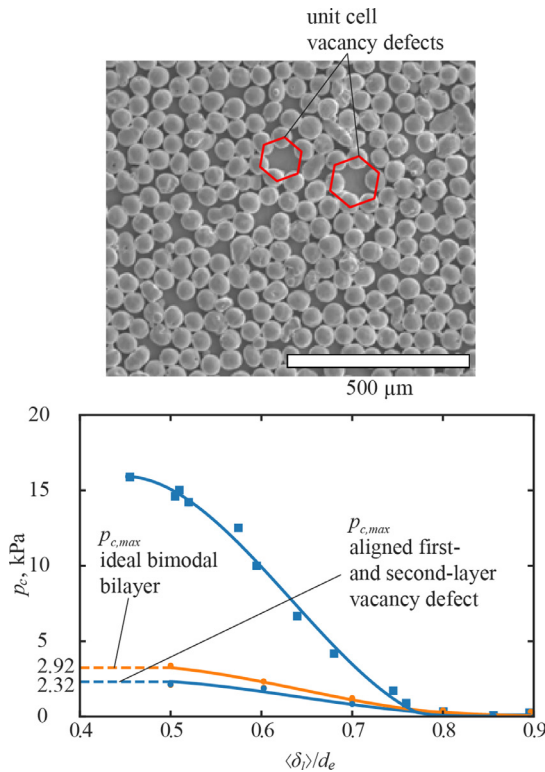


Fig. 5. SEM image of the monolayer wick indicating vacancy defects (heterogeneities).

water; the contact angle is 45°, with smaller particle 50 μm and larger particle 100 μm in diameter.

4. Predicted wick pressure drops

In the FBCW components (Fig. 1), the liquid path from the channel to the heated surface comprises paths through the canopy, and the posts, while spreading and evaporating in the evaporator wick. From the evaporator, the vapor passed through the vapor space, escaped through the perforations, and entered and mixed with the liquid in the channel. The liquid and vapor paths encountered pressure drop through each of these. The combined pressure drops cannot exceed the maximum pressure drop (otherwise capillary-viscous dryout occurs), for example

$$\sum \Delta p_i = \Delta p_e + \Delta p_p + \Delta p_{ca} + \Delta p_{per.g} = p_{c,max}, \quad (6)$$

where the first three terms are the evaporator, post, and canopy wick pressure drop, and last is the vapor pressure drop across the perforation. Each wick pressure drop was calculated by employing the Darcy law (the inertial effects were examined and are negligible) [5]

$$\Delta p_i = \frac{\mu_l \langle u_{l,i} \rangle L_i}{K_i}, \quad i = e, p, ca, \quad (7)$$

where μ_l is the liquid viscosity, $\langle u_l \rangle$ the filtration velocity, and L the path length. The permeability of the post and canopy are estimated by employing the Carman-Kozeny relation [12]

$$K_i = \frac{d_i^2 \epsilon_i^3}{180(1 - \epsilon_i)^2}. \quad (8)$$

For the evaporator wick, the permeability was calculated as a function of the liquid thickness, with the meniscus topology from the SE code, while employing CFD simulations with the Ansys Fluent® [16]. Results for ideal packing and with vacancy defects for the monolayer and bimodal bilayer are indicated in Fig. 6.

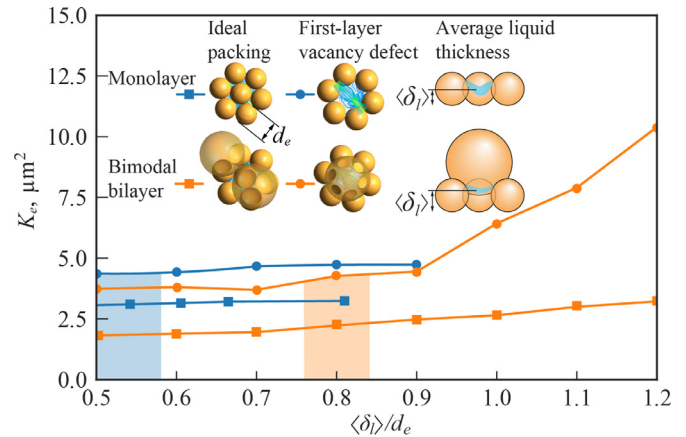
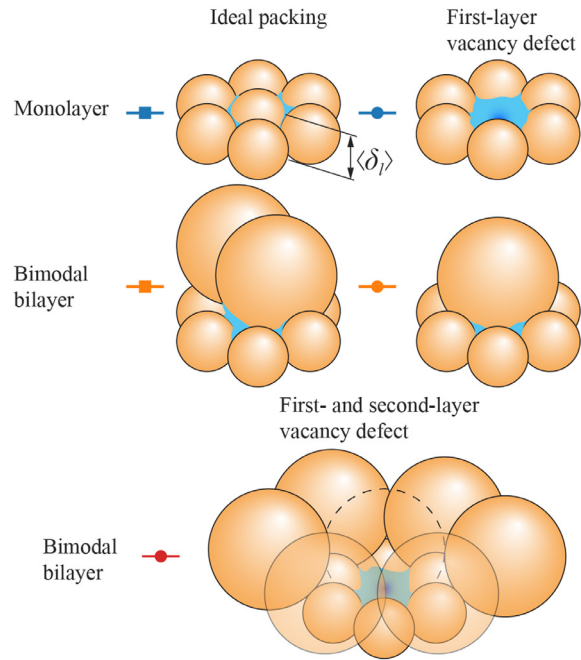


Fig. 6. Variations of permeability with scaled (using the smaller particle diameter) averaged liquid thickness for the monolayer bimodal bilayer with ideal packing and vacancy defect in the first layer. The bilayer allows for larger liquid thickness and larger permeability.

This liquid-thickness-dependent permeability is used along with the maximum capillary pressure [Fig. 5(b)], to calculate the pressure drop in the discretized evaporator wick (allowing for spatial variation in the liquid velocity within the evaporator due to evaporation), employing the resistance network model. The vapor pressure drop across the perforation experienced inertial dominance (examined and determined)

$$\Delta p_{per.g} = \frac{C \rho_g v_g^2}{2}, \quad (9)$$

where ρ_g is the vapor density, v_g the vapor velocity before the perforation, and C the inertial coefficient [17].

The maximum total pressure drop allowed corresponds to the $q_{CHF,c-v}$ limit (controlled by the evaporator maximum capillary

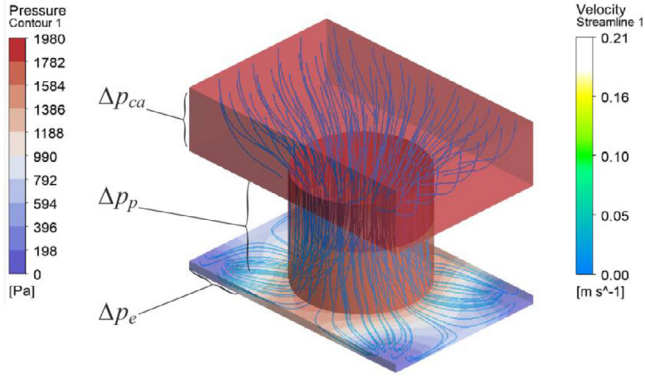


Fig. 7. Snapshot of wick unit cell computational fluid dynamics simulation indicating pressure contour and velocity streamlines inside the wick unit cell for $q = 4.97$ MW/m². Canopy, posts, and evaporator wick pressure drop components are highlighted.

pressure), therefore, Eq. (6) is rewritten to relate the heat flux and the maximum capillary pressure [1], for example

$$\frac{A^* C}{2 \rho_g^2 \Delta h_{lg}} q_{CHF,c-v}^2 + \frac{\mu_l L_p'^2}{\rho_l \Delta h_{lg}} \left[\frac{(L_p' - D_p)/3}{K_e} \frac{4}{(\delta_l)(L_p' + D_p)/2} + \frac{H_p}{K_p D_p^2} \right] q_{CHF,c-v} = p_{c,max} \quad (10)$$

where A^* is the area ratio between the perforation and the evaporator unit cell, D_p and H_p are the post diameter and height, respectively, L_p' is the evaporator unit cell equivalent diameter, K_p and K_e are the post and evaporator permeabilities, and $\langle \delta_l \rangle$ the meniscus thickness in the evaporator. The capillary-viscous CHF, for the monolayer with vacancy defect and bimodal bilayer with a vacancy in the first layer, were calculated with Eq. (10) and provided: $q_{CHF,c-v} = 3.22$ and 4.97 MW/m².

The wick pressure drops were also calculated through CFD simulations with heat flux, equal to the larger capillary-viscous limit $q_{CHF,c-v} = 4.97$ MW/m². The simulations required an exceptionally fine mesh in the evaporator. Results are listed in Fig. 7, with a snapshot indicating the pressure and velocity distributions and streamlines for a unit cell centered around the post. The wick unit cell is 1/6th of the FBCW perforation unit cell, indicated in Fig. 1(b) (2 mm x 3 mm, 0.75 mm thick canopy and 1.3 mm long post with $D_p = 1.5$ mm). The CFD pressure drop results agree with the resistance network model results. The evaporator pressure drop component dominates (attributable to the lower permeability and liquid flow cross-section area) with $\Delta p_e = 1619$, followed by the post, $\Delta p_p = 263$, and canopy, $\Delta p_{ca} = 95$ Pa. The sum of these three components indicated in Fig. 7 equals 1977 Pa, satisfying Eq. (5) with $\Delta p_{per,g} \leq 283$ Pa, again close to the resistance network model predictions.

The component and total pressure drops and the capillary-viscous CHF results for the monolayer and bimodal bilayer evaporator wick are summarized in Table 3, along with the wick parameters, channel geometry, and relevant dimensionless numbers, such as the Reynolds (gas and liquid), Weber, Froude, and Mach numbers [1].

$$\text{Re}_l = \frac{\rho_l u_{l,o} W_{ch}}{\mu_l} \quad \text{Re}_g = \frac{\rho_g v_{g,per} D_{per}}{\mu_g} \quad \text{We}_D = \frac{\rho_l u_{l,o}^2 D_h}{\sigma} \quad \text{Fr}_{D,per} = \left[\frac{\rho_l u_{l,o}^2}{g(\rho_l - \rho_g) D_{per}} \right]^{1/2} \quad \text{Ma}_{g,per} = \frac{v_{g,per}}{u_a} \quad (11)$$

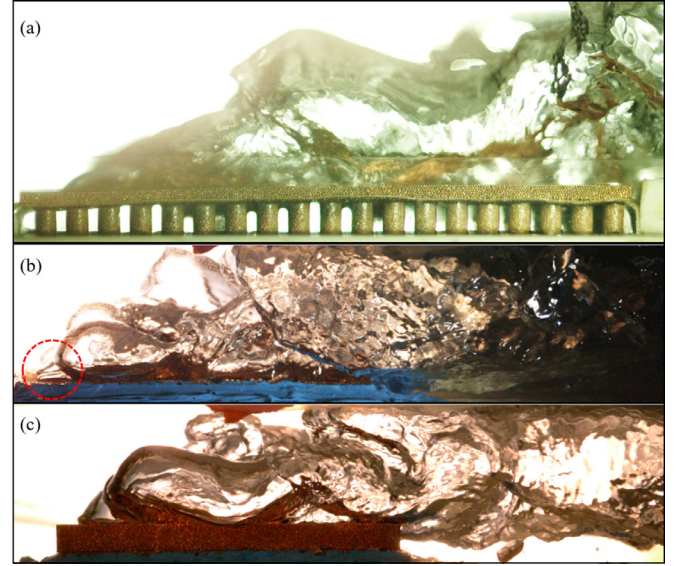


Fig. 8. Video snapshots of the experiment indicating (a) vapor generation in the vapor space (below the canopy), and vapor escape through the perforations; (b) without levees; (c) with levees. The results are for saturated water (1 atm), $q = 2.5$ MW/m², and $u_{l,o} = 0.25$ m/s.

5. Liquid, vapor, and two-phase flows

The FBCW premise is to allow for orderly thin-film evaporation over a thin wick with ensured vapor space above the evaporator wick and lateral liquid supply through the wick. The presented results are for saturated water (one atm) with a liquid velocity of $u_{l,o} = 0.25$ m/s. From the visualization videography, the snapshot in Fig. 8(a) indicates that this liquid flows through the porous posts to the evaporator wick, where it is evaporated. The thin evaporator wick and the vapor space above it led to a large thermal conductance (heat transfer coefficient), allowing reaching dryout limits beyond that recorded for the plain surface.

A corresponding higher liquid supply to the posts is needed to reach these higher dryout limits. The perforated canopy allows for the separation of vapor space from the liquid, flowing through the channel while allowing the vapor to escape steadily. By controlling the perforation spacing and preventing the escaping vapor from shear destabilizing the liquid track, the hydrodynamic CHF is enhanced beyond the plain-surface results. The addition of levees further facilitates this control. This is indicated in the video snapshot of the vapor exiting the perforations, in Fig. 8(b) and (c).

By combining the two-phase flow in the channel and the separated liquid and vapor flows within the FBCW, Fig. 9 indicates these flows comparing the videography of the experiments and the CFD simulation [1] video snapshots. A general agreement exists between the experiments and predictions. The results are for saturated water (one atm), $q = 2.2$ and 2.5 MW/m², and $u_{l,o} = 0.25$ m/s. The FBCW includes the levees. Regarding the experiments, Fig. 9 illustrates the separated channel and wick flows. The vapor from the perforations was prevented from shear destabilizing the established liquid tracks, therefore, removing the otherwise hydrodynamic limit. The liquid-vapor interface in the right of Fig. 9 is represented by the green constant void fraction surface. Under this condition, the capillary-viscous dryout limit, smaller than the hydrodynamic limit [1], controls the dryout.

The CFD simulation domain was limited to two lateral perforations with periodic lateral boundary conditions. This is for computational economy's sake; however, the perforation localized the vapor escape hydrodynamic, therefore, a larger number of lateral

Table 3

A summary of the flow-boiling canopy wick parameters by row: wick components; channel geometry; heat transfer results; dimensionless numbers [18, 19], and pressure drop components; for monolayer and bimodal bilayer with vacancy defects. The results are for saturated water (one atm) with a liquid velocity of $u_{l,o} = 0.25$ m/s.

d_e (μm)	ϵ_e	K_e (μm^2)	d_p (μm)	ϵ_p	K_p (μm^2)	d_{ca} (μm)	ϵ_{ca}	K_{ca} (μm^2)
50	0.41	4.53	150	0.38	17.8	150	0.35	12.7
100,50	0.48	4.06-4.53	150	0.38	17.8	150	0.35	12.7
H_{ch} (mm)	L_{ch} (mm)	W_{ch} (mm)	L_{per} (mm)	H_l (mm)	l_l (mm)	W_{per} (mm)	Δ_p (mm)	$N_{p,x}$
15	39	12	4.5	3	1	1.5	0.5	4
15	39	12	4.5	3	1	1.5	0.5	4
$q_{CHF,c-v}$ (MW/m^2)	G/A ($\text{MW}/\text{m}^2\text{-K}$)	$\langle T_s \rangle - T_{lg}$ (K)	$\Delta T_{sh,max}$ (K)	Re_l	Re_g	$We_{D,c}$	$Fr_{D,h}$	$Ma_{g,per}$
3.22	0.250	13.7	160.4	1.3×10^3	0.5×10^3	6.1	1.68	0.03
4.97	0.250	25.2	160.4	1.3×10^3	1.0×10^3	6.1	1.68	0.03
Δp_{ca} (Pa)	$\Delta p_{per,g}$ (Pa)	Δp_p (Pa)	Δp_e (Pa)	$\sum \Delta p_i$ (Pa)	$p_{c,max}$ (Pa)	Evaporator wick		
41	101	102	2073	2319	2321	Monolayer, with defect		
52	327	158	1784	2319	2321	Bimodal Bilayer, with defect		

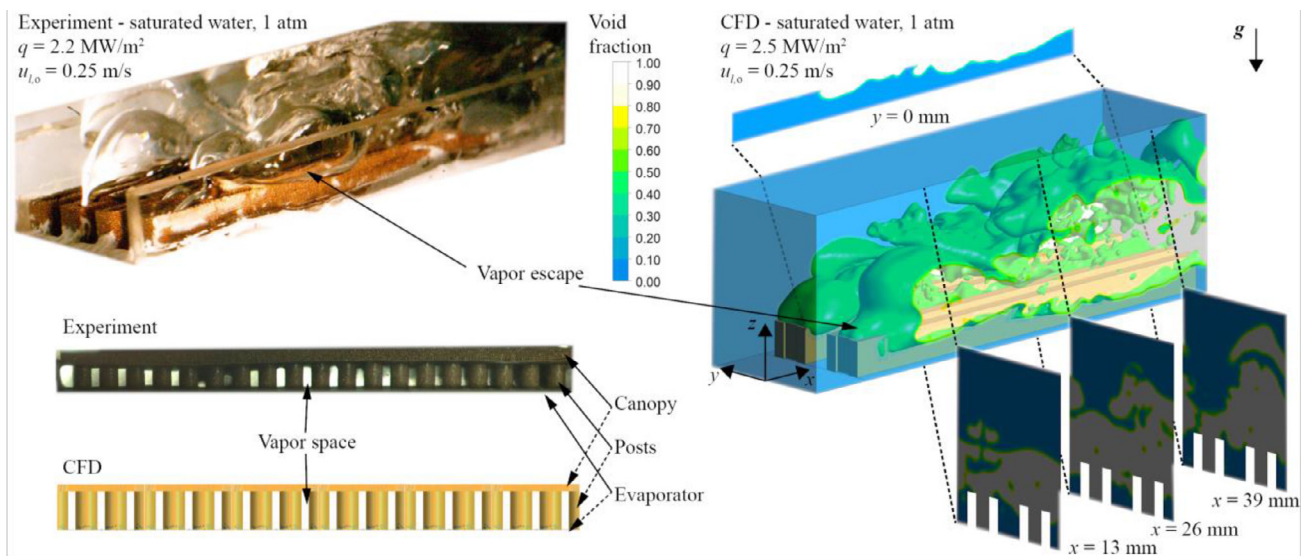


Fig. 9. Comparison of experiments ($q = 2.2$ MW/m^2) and computational fluid dynamics simulations ($q = 2.5$ MW/m^2) snapshots of the flow-boiling canopy wick with levees. The vapor formation in the vapor space (below the canopy) and vapor escape from the canopy (through the perforation among the levees) are evident. The observed and simulated liquid flow through the wick is also presented. The results are for saturated water (1 atm) with $u_{l,o} = 0.25$ m/s. The full video is available in the supplementary materials.

unit cells is not expected to alter the results. The CFD simulation results indicate that the geometrically constrained (by levees) vapor escape successfully, preserves the stability of the liquid tracks while ensuring the continued liquid supply to wick. Both experiments also signify the levees successfully preventing the lateral expansion of vapor, allowing the liquid track to remain undisturbed and postponing dryout to extensively higher heat fluxes. The addition of levees is discussed in [1]. The full video of Fig. 9 is provided in the supplementary materials.

6. Capillary-viscous and hydrodynamic limits

Fig. 10 identifies the saturated water flow boiling experimental results for a liquid velocity of 0.25 m/s, as the variations of the heat flux with the surface superheat. The results are for the plain surface and various FBCW designs with the monolayer and bimodal bilayer evaporator wicks listed in Table 1. The results include the CHF, measured for the plain surface as $q_{CHF,ps} = 1.9$ MW/m^2 . For the plain surface, the CHF is reached with a substantial increase in the surface superheat and this is due to the partial dryout of the surface which increases the average thermal resistance [14]. The results for the monolayer include geometric variations in the post height H_p and post particle diameter d_p . These are listed on the top right of Fig. 10. The highest CHF $q_{CHF,c-v} = 3.6$ MW/m^2 recorded is with the short $H_p = 1.3$ mm and $d_p = 150$

μm . The right of Fig. 10 signifies the predicted pressure drop corresponding to each experiment.

Switching to a bimodal bilayer wick resulted in an additional CHF enhancement, $q_{CHF,h} = 4.6$ MW/m^2 enabled by the increase in K_e (attributable to the larger average liquid layer thickness $\langle \delta_l \rangle$) indicated in Fig. 5. This limit was close to the prediction by Eq. (7) for the same wick, providing $q_{CHF,c-v} = 5.0$ MW/m^2 . This implies that the limitation may be a capillary-viscous limit. These predictions are indicated on the right of Fig. 10.

To reduce the pressure drop across the perforations, the perforation density was increased, reducing the discharge coefficient. The four canopy design variations are discussed in Appendix C, illustrated in Fig. A.3. An incremental increase in the CHF is recorded, raising the limit to $q_{CHF} = 5.1$ MW/m^2 , as expected from the lower total pressure drop. This high perforation density canopy disallows for the addition of levees, though allows for a higher capillary-viscous limit by reducing the vapor velocity exiting the perforation, therefore, reducing the pressure drop there.

The green line on the right (predictions) side of Fig. 10 denotes another feasible improvement to the capillary-viscous limit when the posts lateral spacing $\Delta_{p,y}$ is made equal to the perforation width. The further reduction of the perforation width draws the posts nearer, therefore, reducing the evaporator pressure drop. The main drawback is the increase in the vapor pressure drop, which varies with the square of the heat flux; however, at lower

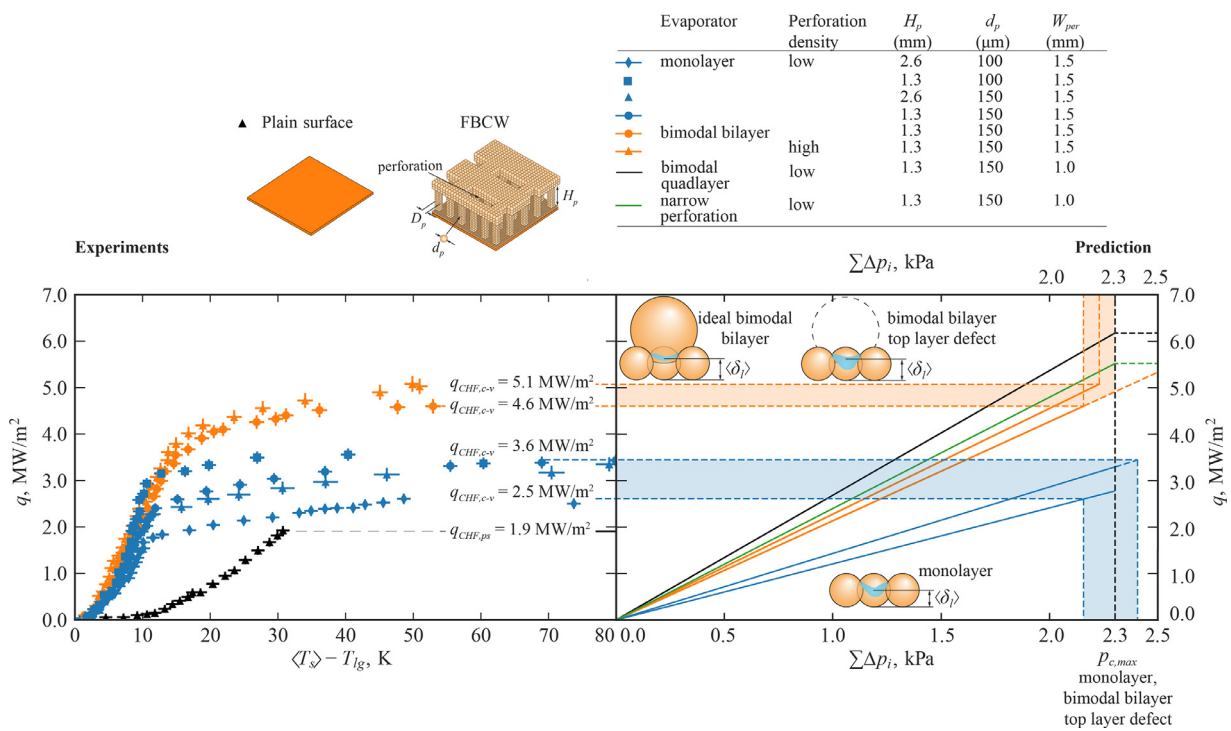


Fig. 10. Evolution of the flow-boiling canopy wick design to enhance the heat flux limit. Left: flow-boiling curve of various FBCW wick designs. Right: variations of capillary-viscous CHF with the total pressure drop for different FBCW wick designs. The results are for saturated (one atm) water with a liquid velocity of 0.25 m/s.

heat flux, this is less than 10% of the total. Reducing the perforation width from 1.5 to 1.0 mm increases the predicted capillary-viscous limit to $q_{CHF,c-v} = 5.5 \text{ MW/m}^2$. Further enhancement can be achieved by utilizing a thicker evaporator layer using smaller particles (for optimal liquid transport by reducing the liquid pressure drop, while increasing the thermal resistance). The capillary-viscous limit with a bimodal quadlayer wick is predicted to have a $q_{CHF,c-v} = 6.3 \text{ MW/m}^2$.

The predicted ideal second-layer packed bimodal bilayer maximum capillary pressure and permeability suggest that [1] the CHF can be further increased. This is indicated with the shaded rectangle on the top right corner of Fig. 10. The error bars correspond to a maximum of 0.2 MW/m² or 4% of the displayed heat flux, and the 1.2°C of the wick superheat. The uncertainty estimates are discussed in Appendix D.

Enhancements of the CHF by addition of a porous structure improving the liquid supply to the heated surface have been reported in [20,21]. A honeycombed (perforated) porous plate is used to allow vapor escape from the perforations. The perforation and wall thickness sizes are controlled similar to the FBCW, albeit the heated surface is facing downward in the liquid channel. The observed enhancements is limited to 1.7 times the plain surface, and their conclusions support the usage of a 3-D capillary evaporator such as the FBCW.

To describe the FBCW hydrodynamic limit, Fig. 11 specifies the evolution of the evaporator, starting with the plain surface with a hydraulic limit $q_{CHF,ps} = 1.9 \text{ MW/m}^2$, slightly above the values reported in the literature [22,23]; however, within the experimental uncertainties. The implementation of the revised interfacial lift-off mechanistic model from [10], discussed at length in Parts I and II, is also within the experimental uncertainty. This hydrodynamic limit increased significantly upon adding the porous posts without the canopy, to $q_{CHF,h} = 3.9 \text{ MW/m}^2$. The liquid flowed in between the posts, affecting the thermal conductance. The hydrodynamic limit was increased to $q_{CHF,h} = 4.6 \text{ MW/m}^2$ upon adding the

canopy on top of the posts. This produced a vapor space beneath the canopy.

A lower perforation density canopy is required for sufficient lateral space between perforations to introduce the levees, with a lower CHF (Fig. 10). The liquid entrainment among posts without the canopy affects the thermal conductance (heat transfer coefficient) G/A . Adding the posts increases G/A to $0.36 \text{ MW/m}^2\text{-K}$. The uncertainty in G/A is derived in Appendix D, established at around 20%. The presence of the canopy creates a vapor space on top of the evaporator, resulting in a significantly small thermal resistance (governed by the thickness of the liquid layer $\langle \delta_l \rangle$ and the effective thermal conductivity of the evaporator $\langle k_e \rangle$, i.e., $G/A = \langle k_e \rangle / \langle \delta_l \rangle$), $G/A = 0.36 \text{ MW/m}^2\text{-K}$. This thermal conductance corresponds to an effective thermal conductivity $\langle k_e \rangle = 14 \text{ W/m-K}$, with the average liquid layer thickness $\langle \delta_l \rangle = 40 \mu\text{m}$, consistent with the correlation for the bulk thermal conductivity of water-copper with a porosity of $\epsilon = 0.4$ [24].

Fig. 11 also denotes the experimental results with the levees. No increase was observed in the dryout limit with the levees within the experimental uncertainties (Appendix D). This supports the premise that the capillary-viscous limit controls the dryout. The thermal conductance (Fig. 11) is $G/A = 0.25 \text{ MW/m}^2\text{-K}$, within the uncertainties. It is concluded that the bimodal bilayer wick (with packing defect) capillary limit was reached.

In Fig. 11 on the right, the experimental results are compared with the CFD simulation results of the channel flow (above the FBCW) [1]. The measured CHF corresponds to a hydrodynamic CHF limit with about 45% of the downstream liquid tracks covered by vapor and preventing the liquid from irrigating the canopy. It is, therefore, suggested that the liquid tracks were not stable enough to irrigate the canopy wick. The CHF was also limited by the hydrodynamic mechanism, which could be raised upon employing the levees, as predicted in [1]. This is evident in Fig. 11.

Fig. 12 indicates time snapshots of the area-averaged liquid track width $\langle w_l \rangle$ at various axial locations (scaled as x/L_{ch}), for heat

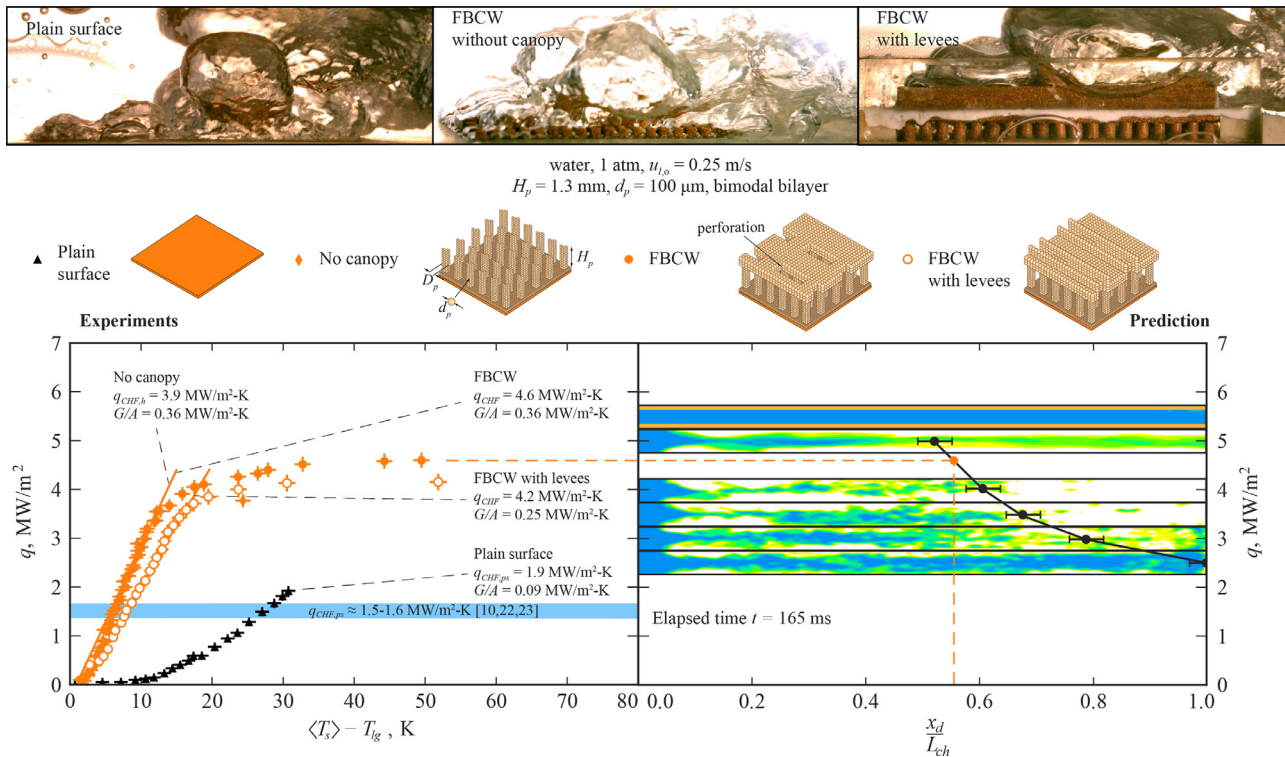


Fig. 11. The experimental results for variations of heat flux with the superheat for the monolayer and bimodal bilayer evaporators. Comparison of experimental results for plain surface and the enhancements obtained with evaporator layer + posts, and evaporator layer + posts + canopy (FBCW). Left: flow boiling curve. Right: CFD snapshots of axial phase distribution immediately above the canopy for FBCW. The visualized video snapshots are also shown on top for the plain and FBCW experiments. The results are for saturated (one atm) water with liquid velocity of 0.25 m/s.

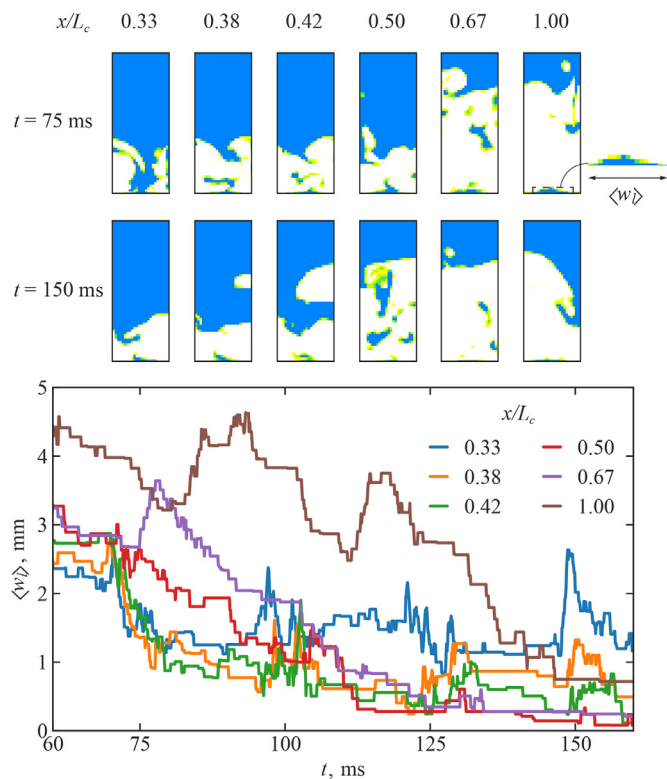


Fig. 12. Time variations of the average liquid track width at various channel locations for $q = 5 \text{ MW/m}^2$ and $u_{l,0} = 0.25 \text{ m/s}$. The corresponding snapshots of liquid-vapor phase distribution are shown on top. The threshold for the local dryout is set to $\langle w_l \rangle = 0.3 \text{ mm}$.

flux $q = 5 \text{ MW/m}^2$ and inlet liquid velocity $u_{l,0} = 0.25 \text{ m/s}$. The liquid track width $\langle w_l \rangle$ measures the extent of the liquid flowing immediately above the canopy, among perforations, as indicated on the top of Fig. 12.

Initially, the influx of vapor shears off the entire liquid track and this is more pronounced in the upstream half of the channel. The snapshots of liquid-vapor phase distribution in the cross-plane, at various axial locations and elapsed times $t = 75$ and 150 ms , illustrate the time evolution of the liquid track width $\langle w_l \rangle(t)$. The threshold for the local dryout of the liquid track is set when $\langle w_l \rangle$ is smaller than 0.3 mm attributable to the adopted image resolution (2% of the image total height.). This is reached for a location downstream midway along the channel ($x/L_{ch} > 0.5$) for $q = 5 \text{ MW/m}^2$.

The liquid track thickness was monitored at the end of the heated section L_{ch} . The dryout and the CHF were based on this exit condition [1]; however, the above comparison with the experiment indicates that partially dried regions continue to sufficiently irrigate the wick. This study, therefore, suggests that the marginal stability theory-based dryout predictions may underestimate the measured CHF. Consequently, in the above experimental results, the surface temperature was measured (extrapolated) at three axial locations and then averaged.

The perforated canopy represents modulated, anisotropic periodic surface vapor venting sites of a wavelength of $\lambda_c = L_{per} + \Delta_{per,x} = 6 \text{ mm}$. According to the interfacial lift-off theory [10], this is the wavelength. The instability led to dryout (boiling crisis); dryout will occur downstream from the distance λ_c from the leading edge. Fig. 13 demonstrates the experimental heat flux and superheat (for $q_{CHF,c-v} = 4.6 \text{ MW/m}^2$) at two thermocouple locations indicated in Fig. 3, $T_{0,1}$ and $T_{0,3}$, located at $x/L_{ch} = 0.25$ and 0.75 , respectively. A top-view schematic of the FBCW is also indicated. The rapid rise in the superheat was first detected at the trailing edge thermocouple site. The accumulated vapor destabilizes the

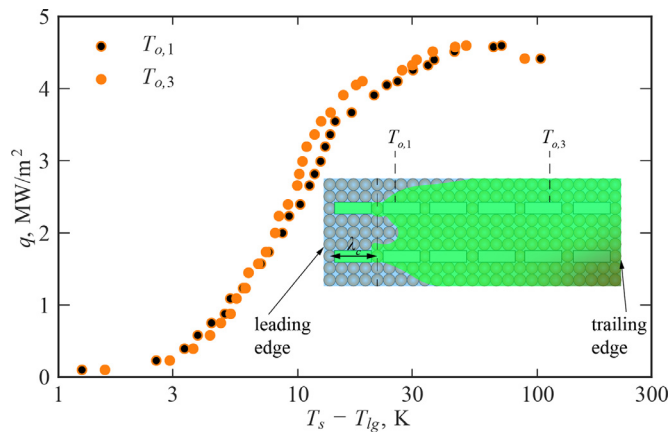


Fig. 13. The axial location dependence of the sudden rise of the surface superheat, indicating the trailing edge locations dryout first. The results are for the bimodal bilayer evaporator test indicated in Fig. 11. A top observation of the liquid track above the canopy is rendered to indicate the trailing edge dryout. The $q_{CHF,c-v} = 4.6 \text{ MW/m}^2$ and $u_{l,o} = 0.25 \text{ m/s}$.

liquid track (or prevents the liquid from wetting the surface) at this downstream location. Both thermocouple locations are within the trailing edge. For better resolution, additional thermocouple sites would have assisted but were not implemented in this study.

The flow-boiling dryout is a leading-edge phenomenon and the heater length, concerning the critical wavelength. It is particularly important in the dryout definition since the downstream accumulation of vapor will eventually lead to dryout (with some regions of partial dryout).

7. Conclusions

The control of the two-phase hydrodynamic boiling crises with capillary surface structures, such as applying the FBCW, offers opportunities to increase the dryout limit (CHF) and the thermal conductance. These controls also allow for further examination of the fundamentals of the flow-boiling crisis. As the heat flux limit increases, the eminent crisis controlling mechanism becomes the capillary-viscous limit, compared to the hydrodynamic, wick superheat, and vapor choking, among other things. By using saturated water, the sintered-copper FBCW was designed, and fabricated was assessed in a flow-boiling loop. It is indicated that the bimodal bilayer evaporator wick can provide a higher maximum capillary pressure. The FBCW 3-D architecture is optimized for the minimum pressure drops.

The study demonstrated that the FBCW increases the hydrodynamic limit over the plain surface. The separation between the channel and the wick flows helps increase this further over that of the modulated wick (FBCW without the perforated canopy wick). By adding the stabilizing levees on the FBCW, predicted to increase the dryout limit further [1], it is observed that the capillary-viscous limit $q_{CHF,c-v} = 4.6 \text{ MW/m}^2$ is reached (the limit on the capillary suction). By optimizing the FBCW geometry, a slightly higher dryout was expected by using a smaller perforation width. To increase the dryout limit, the wick capillary-viscous limit should be raised with larger capillary suction and smaller pressure drops. The thermal conductance of the FBCW was also large, $G/A = 0.36 \text{ MW/m}^2\text{-K}$.

The predicted $q_{CHF,c-v}$ limit (Section 4) depends on the evaporator wick maximum capillary pressure estimated in Section 3; the results are within the uncertainty of the experimental results. It is concluded that the assumptions in Sections 3 and 4 are thorough, supported by the SEM images of the evaporator wick. The current challenge is to eliminate the occurrence of vacancy defects

in the evaporator wick fabrication, therefore, increasing the maximum capillary pressure, using the bimodal bilayer wick which increases the permeability.

The videography flow visualization of the experiments illustrates the FBCW operation with complete separation of the near-(wick and vapor space) and far-field (channel, two-phase) flows. The CFD simulations confirm the vapor escape and two-phase flow in the channel observed in experiments, supporting hydrodynamic limits in the assessments.

The pool-boiling hydrodynamic instability theory is based on rising surface vapor columns in a staggered arrangement in a unit cell. In flow boiling, the forced flow, and its direction, u_l , create a leading-edge region, complementing the pool-boiling, phase-buoyancy vertical counter-flowing liquid supply to the surface. Depending on u_l , the flow boiling increases the hydrodynamic dryout heat flux limit over the pool-boiling CHF. With the CFD-VOF direct simulations [1] the effect u_l , on this hydrodynamic CHF was examined, by using the FBCW surface vapor column (perforation) control. This supports a more stable surface liquid track, increasing the hydrodynamic dryout heat flux limit (the local dryout occurs further downstream). Here this vapor-venting site's control was demonstrated, with an optimized porous surface coating, indicating the FBCW. Further FBCW optimization, including its maximum capillary pressure, is needed to reach the predicted high $q_{CHF,h}$.

Supplementary materials

Videos of the flow-boiling with the FBCW indicating the (a) side view at https://youtu.be/HDNnwr8_SnA, and (b) at the oblique view at <https://youtu.be/nO4bqwtA-ZI>. The results are for saturated (one atm) water with liquid inlet velocity $u_{l,o} = 0.25 \text{ m/s}$ with (a) $q = 2.2 \text{ MW/m}^2$, and (b) $q = 1.7 \text{ MW/m}^2$.

The Fig. 9 video is at <https://youtu.be/OeYti5EcVgc>.

Declaration of Competing Interest

The authors declare that they have no known competing financial interests or personal relationships that could have appeared to influence the work reported in this paper.

CRedit authorship contribution statement

Tong Kyun Kim: Investigation, Data curation, Conceptualization, Visualization. **Julio Ferreira:** Software, Formal analysis, Visualization, Writing – review & editing. **Hangjin Jo:** Writing – review & editing, Supervision, Resources, Funding acquisition. **Massoud Kaviani:** Conceptualization, Methodology, Supervision, Writing – review & editing, Project administration.

Acknowledgments

TKK and HJJ are grateful for support in the form of a National Research Foundation of South Korea (NRF) grant, funded by the Korean Government (MSIP) (NRF-2017M1A7A1A03072765). MK is grateful for support from NSF USA (Thermal Transport and Processes, CBET16235720). JF is thankful, acknowledging his scholarship supported by CAPES-Brazilian Federal Agency for Support and Evaluation of Graduate Education, within the Ministry of Education (88881.170629/2018-01).

We are indebted to Prof. Moo Hwan Kim (Currently, President of Pohang University of Science and Technology) for his visionary initiation and support of this collaborative research.

Our appreciation to our copyeditor, Ms. Elizabeth Marx, representing Academic and Professional Editing Services (APES) for her input in editing and formatting this manuscript.

Supplementary materials

Supplementary material associated with this article can be found, in the online version, at doi:[10.1016/j.ijheatmasstransfer.2021.121999](https://doi.org/10.1016/j.ijheatmasstransfer.2021.121999).

Appendices: Experiment methods

Appendix A: Mold-furnace sintering

Fig. A.1 represents the mold-furnace FBCW fabrication steps for each four wick component.

A.1 Plain surface

The plain surface is a mechanically polished copper substrate, using abrasive paper (#220, #1000, and #1500), signified in Fig. 2(a); the surface was cleaned with a variation of ethanol, acetone, and water.

A.2 Evaporator

The monolayer is a single layer of 50 μm spherical copper particles on the plain surface (Fig. 2(b)). It is deposited by employing the Langmuir-Blodgett Film method [25]. This floats the particles on the water surface by lowering the water level deposit to a single particle layer on the surface (Fig. A.1(a)). A second 100 μm particle layer is formed on top of the monolayer for the bimodal bilayer evaporator (Fig. 2(c)), following the deposit and sintering of the 100 μm spherical copper particles above the monolayer with the same method used for the monolayer.

A.3 Posts

Posts are constructed of 100 μm or 150 μm spherical copper particles (Fig. 2(d)). The fabrication steps involve filling the post graphite mold with the particles, positioning the evaporator on top of the post graphite mold, followed by sintering and removing the graphite mold, Fig. A.1(b).

A.4 Perforated canopy

The canopy comprises 150 μm spherical copper particles (Fig. 2(e)). The fabrication steps are placing the particles in the canopy graphite mold, using the structure composed to the posts on top of it (upside down), and sintering Fig. A.1(c).

A.5 Levees

Levees comprise 150 μm spherical copper particles (Fig. 1(f)); the steps are sintering particles in the levees' graphite mold. The levees were positioned on an FBCW canopy Fig. A.1(d).

Appendix B: Flow-boiling loop

Fig. A.2 represents the flow-boiling where the DI water was used. The experiments were conducted under one atm and 0 to 17000 Pa gauge pressure; mostly under a liquid mass flow rate of 250 $\text{kg}/\text{m}^2\text{-s}$, with small liquid inlet subcooling (3–9°C). The liquid from the pool passes through the flow meter and preheater and test channel with one transparent (glass) sidewall, subsequently passing through the condenser, returning to the pool. The liquid flow rate was measured with a turbine flow sensor (GMP, NURITECH). The flow was controlled with a pump and a needle valve. During the experiment, a preheater (13 kW) and a (PID) controller (TZ4ST, Autonics) controlled the fluid temperature. A K-type thermocouple and pressure gauge (PX01C1-300GV, Omega) measured the temperature and pressure at the channel inlet and outlet. A PI controlling the cartridge heaters (12 kW total) in the copper block, determined the heat flux. The data acquisition system (34970a, Agilent) collected the flow rate, temperature, pressure, and heat flux at 1 s intervals.

Appendix C: Flow-boiling canopy wick design variations

Fig. A.3 denotes FBCW design variations employed in the experiments. The first design lacked a canopy, such as the sintered evaporator and posts on top of the copper plate (Fig. A.3(a)). The canopy was added in the full FBCW with the 4 \times 6 perforations (low density) Fig. A.3(b)). The high-density perforation comprised 7 \times 6 perforations (Fig. A.3(c)). Finally, the FBCW with levees is shown, using the low-density perforation, since the high-density perforation has lateral inter-perforation spacing, too small to allow placing levees there (Fig. A.3(d)). The levees diverted the vapor away from the liquid track above the canopy, allowing for a higher hydrodynamic dryout limit [1].

Table A.1 summarizes the FBCW geometric variations occupied in the experiments.

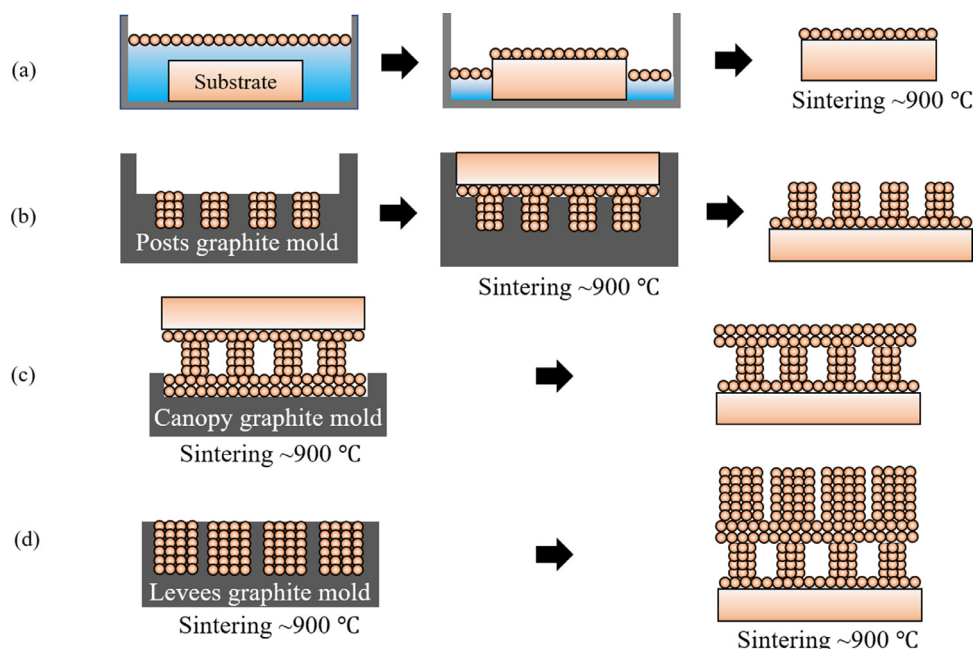


Fig. A.1. The progressive steps in the flow-boiling canopy wick fabrication. (a) Monolayer; (b) posts; (c) canopy; and (d) levees.

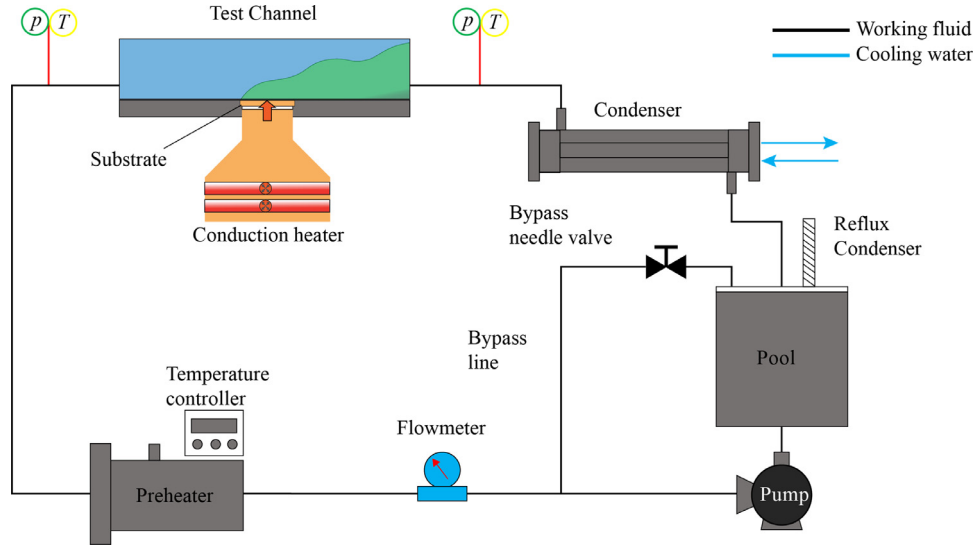


Fig. A.2. Schematic of the flow-boiling loop, specifying the components.

Table A.1 Geometric parameters of the varied flow-boiling canopy wick designs.

Design	H_p (mm)	D_p (mm)	$\Delta_{p,x}$ (mm)	$\Delta_{p,y}$ (mm)	$\Delta_{p,y-e}$ (mm)	H_{ca} (mm)	$\Delta_{per,y}$ (mm)	W_{per} (mm)	L_{per} (mm)	H_l (mm)	l_l (mm)
No canopy	1.3	1.5	0.5	1.5	0.75	1	4.5	1.5	4.5	-	-
FBCW low-density perforation	1.3	1.5	0.5	1.5	0.75	1	4.5	1.5	4.5	-	-
FBCW high-density perforation	1.3	1.5	0.5	1.5	0.75	1	3	1.5	4.5	-	-
FBCW with levees	1.3	1.5	0.5	1.5	0.75	1	4.5	1.5	4.5	5	1

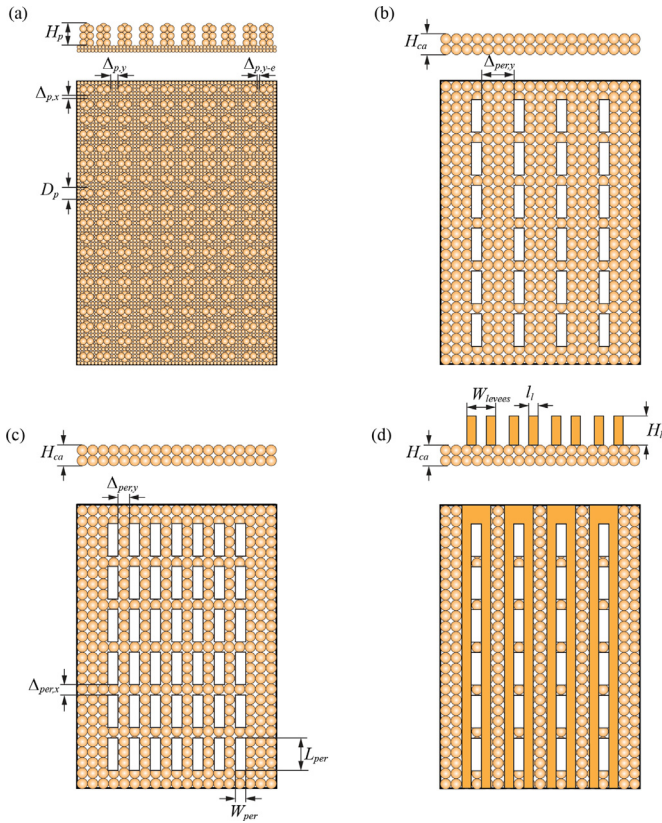


Fig. A.3. Various flow-boiling canopy wick designs (a) No canopy; (b) Low-density perforation canopy wick with 4×6 perforations, CS; (c) High-density perforation canopy wick with 7×6 perforations, CM; (d) Low-density perforation canopy wick with levees.

Appendix D: Experimental uncertainty estimation

The uncertainty sources of a measured parameter X can be defined as systematic (statistical bias) or random. The systematic uncertainty b_X explains uncertainties regarding the measurement instrument or method, diminished by calibration procedures. The random uncertainty s_X conversely, justifies random sources [26, 27]. The combined uncertainty of X is then calculated as

$$u_X^2 = b_X^2 + s_X^2, \quad (A.1)$$

where s_X is often approximated as the sample standard deviation. When dealing with a derived parameter $R = f(X_1, X_2, \dots, X_k)$, its combined uncertainty can be calculated by the uncertainty propagation method [26]

$$u_R = \left[\sum_{j=1}^k \left(\frac{\partial R}{\partial X_j} \right)^2 u_{X,j}^2 \right]^{1/2}. \quad (A.2)$$

The uncertainty reported is the expanded uncertainty

$$U_R = K_r u_r, \quad (A.3)$$

where K_r is the coverage factor, a number representative of the confidence interval associated with the reported uncertainty. A confidence interval of 95% is commonly used; for a large number of measurements, $K_r = 1.96$. If the coverage factor is concealed in the manufacturer's datasheet, a rectangular distribution is assumed $K_r = 1.73$.

The uncertainties for the heat flux and thermal resistance are now derived. The heat flux is calculated employing the electrical power method as

$$q = \eta_e \frac{Q}{A} = \eta_e \frac{\Delta\varphi^2}{R_e} \frac{1}{A}, \quad (A.4)$$

where η_e is the effectiveness of heat absorption, $\Delta\varphi$ is the voltage, R_e is the electric resistance, A is the heater block area.

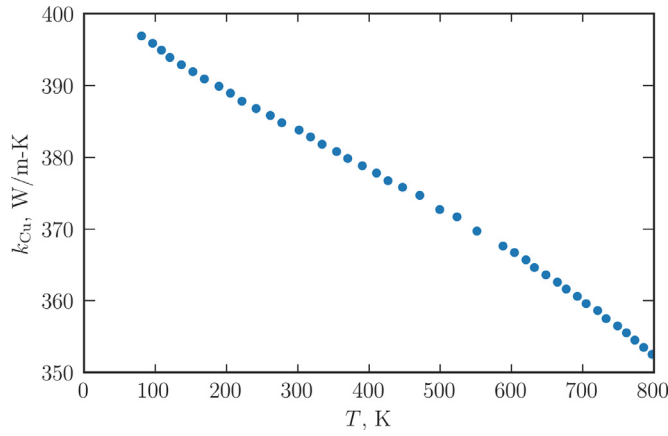


Fig. A.4. Variations of the copper thermal conductivity concerning temperature [28].

If the conduction method was used instead, the heat flux would be calculated as

$$q = \frac{k_{Cu}(T_{Cu,2} - T_{Cu,1})}{L}, \quad (A.5)$$

where k_{Cu} is the thermal conductivity of copper, L is the distance between the two thermocouples inside the block and $T_{Cu,i}$ is the temperature measured in the block.

By employing Eq. (A.4) (electrical power method), the combined uncertainty expression for the heat flux is derived

$$u_q = \left[\left(\eta_e \frac{2\Delta\varphi}{R_e A} \right)^2 u_V^2 + \left(\eta_e \frac{\Delta\varphi^2}{R_e^2 A} \right)^2 u_{R_e}^2 + \left(\eta_e \frac{\Delta\varphi^2}{R_e A^2} \right)^2 u_A^2 \right]^{1/2}, \quad (A.6)$$

where u_A is the uncertainty of the heater block cross-sectional area $A = LW$

$$u_A = [W^2 u_L^2 + L^2 u_W^2]^{1/2}, \quad (A.7)$$

where L and W are the length and width, respectively.

Similarly, by employing Eq. (A.5) (conduction method), the following expression for the combined uncertainty is derived.

$$u_q = \left[\left[\frac{(T_{Cu,2} - T_{Cu,1})}{L} \right]^2 u_k^2 + \left(\frac{k_{Cu}}{L} \right)^2 u_T^2 + \left[\frac{k_{Cu}(T_{Cu,2} - T_{Cu,1})}{L^2} \right]^2 u_L^2 \right]^{1/2}, \quad (A.8)$$

where u_k is the thermal conductivity uncertainty and u_L is the thermocouple distance uncertainty.

The thermal conductivity of copper is calculated employing the data in Fig. A.4 and the associated uncertainty is

$$u_k = \left[\frac{\sum (k_{Cu} - k)^2}{N - (1 + M)} \right]^{1/2}, \quad (A.9)$$

where $k_{Cu}(T)$ is from Fig. A.4 data, $k(T) = AT + B$ is the linear curve fit with $N = 42$ as the number of data points and $M = 1$ as the order of the polynomial fit.

The global conductance G/A is defined as

$$\frac{G}{A} = \frac{q}{T_s - T_{lg}} = \frac{q}{\frac{1}{3} \sum_{i=1}^3 (T_{o,i} - \frac{q}{k_{Cu}} L_s) - T_{lg}}, \quad (A.10)$$

Table A.2

Expanded uncertainties for $K_r = 1.96$ (95%).

U_T (K)	0.5	$U_{\Delta\varphi}$ (V)	0.08	U_{GA} (W/m ² -K)	0.08
U_p (kPa)	2.03	U_{R_e} (Ω)	0.006	$U_{T_{lg}}$ (K)	0.5
U_L (mm)	0.20	U_q (MW/m ²)	0.08-0.16		
U_A (mm ²)	2140	U_k (W/m-K)	1.37		

Therefore, combined uncertainty is

$$u_{GA} = \left[\left(\frac{\frac{1}{3} \sum_{i=1}^3 T_{o,i} - T_{lg}}{\frac{1}{3} \sum_{i=1}^3 (T_{o,i} - \frac{q}{k_{Cu}} L_s) - T_{lg}} \right)^2 u_q^2 + \left\{ \frac{q}{\left[\frac{1}{3} \sum_{i=1}^3 (T_{o,i} - \frac{q}{k_{Cu}} L_s) - T_{lg} \right]^2} \right\}^2 u_T^2 + \left\{ \frac{q}{\left[\frac{1}{3} \sum_{i=1}^3 (T_{o,i} - \frac{q}{k_{Cu}} L_s) - T_{lg} \right]^2} \right\}^2 u_{T_{lg}}^2 \right]^{1/2}, \quad (A.11)$$

where u_{T_s} is the uncertainty of the temperature measuring device and $u_{T_{lg}}$ is the uncertainty of the saturation temperature, calculated as

$$u_{T_{lg}} = \left[\left(\frac{\partial T_{lg}}{\partial p} \right)^2 u_p^2 + u_{EOS}^2 \right]^{1/2}, \quad (A.12)$$

where u_p is the pressure measurement uncertainty, u_{EOS} is the uncertainty of the employed equation of states. Usually, it is of a higher order than the other two, therefore, it can be safely neglected. The differential term in Eq. (A.12) can be approximated with the forward differential scheme

$$\frac{\partial T_{lg}}{\partial p} = \lim_{\Delta p \rightarrow 0} \frac{T_{lg}(p + \Delta p) - T_{lg}(p)}{\Delta p}. \quad (A.13)$$

The measured and derived expanded uncertainties are indicated in Table A.2. These heat flux and temperature uncertainties are marked as error bars in Fig. 10 and Fig. 11.

References

- [1] J. Ferreira, M. Kaviany, Geometric-confinement suppression of flow-boiling instability using perforated wick: Part I CHF and conductance enhancement, *Int. J. Heat Mass Transf.* 159 (2020) 12080.
- [2] J. Ferreira, M. Kaviany, Geometric-confinement suppression of flow-boiling instability using perforated wick: Part II CHF limits and wick properties, *Int. J. Heat Mass Transf.* 159 (2020) 120079.
- [3] N. Zuber, *Hydrodynamic aspects of boiling heat transfer*, University of California, Los Angeles, 1959.
- [4] V. Sernas, J. Lienhard, V. Dhir, The Taylor wave configuration during boiling from a flat plate, *Int. J. Heat Mass Transf.* 16 (9) (1973) 1820–1821.
- [5] J.H. Lienhard, V.K. Dhir, Hydrodynamic prediction of peak pool-boiling heat fluxes from finite bodies, *ASME J. Heat Transf. Ser. C* 95 (1973) 152–158.
- [6] S. Liter, M. Kaviany, Pool-boiling CHF enhancement by modulated porous-layer coating: theory and experiment, *Int. J. Heat Mass Transf.* 44 (2001) 4287–4311.
- [7] M. Bruder, G. Bloch, T. Sattelmayer, Critical heat flux in flow boiling—review of the current understanding and experimental approaches, *Heat Transf. Eng.* 38 (3) (2016) 347–360.
- [8] C. Konishi, I. Mudawar, Review of flow boiling and critical heat flux in microgravity, *Int. J. Heat Mass Transf.* 80 (2015) 469–493.
- [9] J.E. Galloway, I. Mudawar, CHF mechanism in flow boiling from a short heated wall - I. Examination of near-wall conditions with the aid of photomicrography and high-speed video imaging, *Int. J. Heat Mass Transf.* 36 (1993) 2511–2526.
- [10] C.-N. Huang, C.R. Kharangate, A new mechanistic model for predicting flow boiling critical heat flux based on hydrodynamic instabilities, *Int. J. Heat Mass Transf.* 138 (2019) 1295–1309.
- [11] N. Albu, G. Hwang, Bimodal thin wick structures for high heat flux two-phase thermal control systems, in: *Proceedings of the International Conference on Environmental Systems*, 2019.

- [12] M. Kaviany, *Principles of Heat Transfer in Porous Media*, Springer, New York, 1995.
- [13] K. Brakke, The surface evolver, *Exp. Math.* 1 (1992) 141–165.
- [14] G.S. Hwang, Y. Nam, E. Fleming, P. Dussinger, Y.S. Ju, M. Kaviany, Multi-artery heat pipe spreader: Experiment, *Int. J. Heat Mass Transf.* 3 (13-14) (2010) 2662–2669.
- [15] S. Modak, M. Kaviany, S. Hoenig, R. Bonner, Numerical analysis of meniscus dynamics in monolayer-wickdropwise condensation, *Numer. Heat Transf. Part A Appl.* 76 (2019) 301–322.
- [16] ANSYS, "Fluent reference manual," 2009. [Online]. Available: https://www.afs.enea.it/project/neptunius/docs/fluent/html/ug/main_pre.htm. [Accessed 21 October 2020].
- [17] A. Ward-Smith, *Internal Fluid Flow: The Fluid Dynamics of Flow in Pipes and Ducts*, Oxford University Press, London, 1980.
- [18] Y. Murai, Frictional drag reduction by bubble injection, *Exp. Fluids* 55 (2014) 1773, doi:10.1007/s00348-014-1773-x.
- [19] D. Kim, P. Moin, Direct numerical study of air layer drag reduction phenomenon over a backward-facing step, *Cent. Turbul. Res. Annu. Res. Brief.* (2010) 351–363.
- [20] L. Wang, A. Khan, N. Erkan, H. Gong, K. Okamoto, Critical heat flux enhancement on a downward face using porous honeycomb plate in saturated flow boiling, *Int. J. Heat Mass Transf.* 109 (2017) 454–461.
- [21] L. Wang, Y. Yuan, N. Erkan, F. Li, K. Okamoto, Effect of metal honeycomb structure on enhancing CHF in saturated downward-facing flow boiling, *Int. J. Heat Mass Transf.* 149 (2020) 119244.
- [22] T. Lee, D.H. Kam, H.H. Lee, Y.H. Jeong, Effects of two-phase flow conditions on flow boiling CHF enhancement of magnetite-water nanofluids, *Int. J. Heat Mass Transf.* 74 (2014) 278–284.
- [23] P. Weber, K. Johannsen, Study of the critical heat flux condition at convective boiling of water: temperature and power-controlled experiments, in: *Proceedings of the 9th International Heat Transfer Conference*, New York, 1990.
- [24] G. Hadley, Thermal conductivity of packed metal powders, *Int. J. Heat Mass Transf.* 29 (6) (1986) 909–920.
- [25] O. Oliveira, Langmuir-blodgett films-properties and possible applications, *Braz. J. Phys.* 22 (2) (1992) 60–69.
- [26] R. Moffat, Describing the uncertainties in experimental results, *Exp. Therm. Fluid Sci.* 1 (1988) 3–17.
- [27] H. Coleman, W. Steele, *Experimentation, Validation, and Uncertainty Analysis for Engineers*, 3rd ed., John Wiley & Sons, New Jersey, 2009.
- [28] T.W. Davies, Thermal conductivity values. A-to-Z guide to thermodynamics, heat and mass transfer, and fluids engineering, *Thermopedia* (2006) [Online]. Available: https://dx.doi.org/10.1615/AtoZ.t.thermal_conductivity_values. [Accessed 18 March 2021].